Interface-independent sound speed and thermal conductivity of atomic-layer-deposition-grown amorphous AlN/Al_2O_3 multilayers with varying oxygen composition

Md Shafkat Bin Hoque,[1] Ian A. Brummel,[2] Eric R. Hoglund,[2] C. Jaymes Dionne,[3] Kiumars Aryana,[1] John A. Tomko,[1] John T. Gaskins,[4] Daniel Hirt,[1] Sean W. Smith,[5] Thomas Beechem,[6] James M. Howe,[2] Ashutosh Giri,[3] Jon F. Ihlefeld,[2,7] and Patrick E. Hopkins[1,2,8,*]

[1]*Department of Mechanical and Aerospace Engineering, University of Virginia, Charlottesville, Virginia 22904, USA*
[2]*Department of Materials Science and Engineering, University of Virginia, Charlottesville, Virginia 22904, USA*
[3]*Department of Mechanical, Industrial and Systems Engineering, University of Rhode Island, Rhode Island 02881, USA*
[4]*Laser Thermal Analysis, Charlottesville, Virginia 22902, USA*
[5]*Radiant Technologies, Albuquerque, New Mexico 87107, USA*
[6]*School of Mechanical Engineering and Birck Nanotechnology Center, Purdue University, West Lafayette, Indiana 47907, USA*
[7]*Charles L. Brown Department of Electrical and Computer Engineering, University of Virginia, Charlottesville, Virginia 22904, USA*
[8]*Department of Physics, University of Virginia, Charlottesville, Virginia 22904, USA*

(Received 3 July 2022; accepted 4 January 2023; published 2 February 2023)

Dielectric amorphous multilayers (AMLs) play a critical role in a wide array of technologies such as optical coatings, nanoelectronics, energy harvesting, and recovery devices. However, despite their wide applications, a robust understanding of the effect of the interplay between chemical and structural disorder on the thermal properties of AMLs is still lacking. Therefore, in this paper, we experimentally and numerically investigate the effects of composition and interface density on the sound speed and thermal conductivity of a series of amorphous aluminum nitride and aluminum oxide multilayers grown via plasma-enhanced atomic layer deposition. To systematically change the composition, the oxygen content of the AMLs is proportionally varied with interface density during growth. We find that the longitudinal sound speed of these AMLs is dictated by the oxygen content instead of the number of interfaces. The thermal conductivity, in contrast, is dictated by both interface density and oxygen content. The interfaces act to decrease the thermal conductivity, whereas the oxygen content increases the thermal conductivity. Due to the competing influence of the interfaces and oxygen content, the thermal conductivity of the AMLs remains nearly constant as a function of interface density. Our study provides crucial insights into the effect of the interplay of composition and interfaces on the sound speed and thermal conductivity of AMLs.

DOI: 10.1103/PhysRevMaterials.7.025401

I. INTRODUCTION

Amorphous multilayers (AMLs) are widely used for thermal, optical, and mechanical coatings [1,2], optoelectronics [3,4], thermoelectrics [5–9], and microelectronic devices [10]. However, compared with their crystalline counterparts, the vibrational thermal transport mechanisms of AMLs are still not well understood. In contrast to the phonons in crystalline superlattices, multiple vibrational modes such as propagons (delocalized, propagating modes), diffusons (delocalized, nonpropagating modes), and locons (localized, nonpropagating modes) dictate the thermal transport of AMLs [11–14]. Unlike a crystalline superlattice, the thermal conductivity of an AML can be expressed by a thermal circuit model where the total resistance of an AML is the superposition of the resistances provided by the individual layers and interfaces [15,16].

A large number of studies have investigated the role of interfaces on the thermal conductivity of AMLs. Ali *et al.* [17] reported that increasing the number of interfaces (defined by interface density) reduced the thermal conductivity of amorphous Al_2O_3/TiO_2 multilayers up to a certain extent, after which the thermal conductivity became constant. A similar trend was also noticed in Si/Ge AMLs [18]. These works showed that the interfaces play a non-negligible role in the thermal conductivity of AMLs. Such thermal conductivity reduction due to the presence of a large number of interfaces is highly undesirable for microelectronic applications where waste heat needs to be quickly dissipated. Recently, Giri *et al.* [15] showed that this issue can be mitigated via interfacial defects. The introduction of nitrogen defects at the SiOC:H/SiC:H interfaces caused the thermal conductivity of the AMLs to become independent of interface density. Such behavior is particularly intriguing considering that the thermal properties of many amorphous materials can be tuned via stoichiometry [19,20]. Together, these findings motivate us to investigate the impact of compositional change on the thermal conductivity of an AML. Additionally, it is of significant interest to study the effect of such compositional change on the sound speed of AMLs. In crystalline materials, the thermal conductivity usually scales with sound speed [21,22]. As the

*phopkins@virginia.edu

 ©2023 American Physical Society

TABLE I. Structural and chemical compositions of the AMLs and control films along with the measured sound speed and thermal conductivities. The period and film thicknesses of the samples are measured via TEM and have an uncertainty of ∼3%.

Specimens	Film thickness (nm)	Oxygen content (at. %)	Longitudinal sound speed (m/s)	Thermal conductivity ($W\,m^{-1}\,K^{-1}$)
a-AlN control films	48	0	6370 ± 547	0.94 ± 0.1
	81			
a-Al_2O_3 control films	86	100	8747 ± 328	2.1 ± 0.23
	104			
22-nm-period AML	109	57.5	7413 ± 235	1.45 ± 0.1
10-nm-period AML	106	62.4	7717 ± 304	1.68 ± 0.13
5-nm-period AML	101	71.5	7962 ± 310	1.61 ± 0.13
2.4-nm-period AML	95	94	8184 ± 395	1.58 ± 0.13

vibrational thermal transport mechanisms of AMLs are completely different from crystalline ones, the possibility exists for deviation from the aforementioned trend in AMLs. Therefore a systematic study on the interplay between vibrational scattering and the structural and chemical disorder inherent to an AML is highly warranted.

Towards this goal, we study the sound speed and thermal conductivity of a series of amorphous aluminum nitride/aluminum oxide (AlN/Al_2O_3) multilayers grown via plasma-enhanced atomic layer deposition. The presence of oxygen in the deposition chamber during the growth causes oxidation of the AlN layers. As a result, the oxygen content of the amorphous AlN/Al_2O_3 multilayers linearly varies with interface density. Our measurements reveal that such compositional change gives rise to different trends in longitudinal sound speed and thermal conductivity. The longitudinal sound speed of the multilayers linearly increases with oxygen content irrespective of interface density. This happens as the Al-O bond is stronger than the Al-N bond. The thermal conductivity of the AMLs, on the other hand, remains nearly constant as a function of both interface density and oxygen content and is an average of the thermal conductivities of amorphous aluminum nitride (a-AlN) and aluminum oxide (a-Al_2O_3). We posit that this trend in AML thermal conductivity stems from the simultaneous occurrence of two opposing thermal transport mechanisms. The increase in interface density leads to a decrease in thermal conductivity. In contrast, the increasing oxygen content leads to an increase in thermal conductivity due to the relatively higher thermal conductivity of a-Al_2O_3. We verify our hypothesis by performing molecular dynamics (MD) simulations on a representative AML system. Thus, in addition to providing fundamental insights into the vibrational thermal transport mechanisms, our study opens up pathways for tuning thermal properties of AMLs.

II. GROWTH DETAILS OF THE AlN/Al_2O_3 MULTILAYER FILMS

In this paper, we grow four amorphous AlN/Al_2O_3 multilayers along with two a-AlN and two a-Al_2O_3 control films via plasma-enhanced atomic layer deposition (PE-ALD; FlexAL II, Oxford Instruments) on lightly doped, *p*-type (001)-orientation silicon (Si) wafers (University Wafers). The AlN/Al_2O_3 multilayers are grown in period thicknesses of 22, 10, 5, and 2.4 nm with final film thicknesses of 109, 106, 101, and 95 nm, respectively. The thicknesses of the two control a-AlN samples are 48 and 81 nm, whereas for the a-Al_2O_3 films, the thicknesses are 86 and 104 nm. Tetramethyl aluminum precursor in conjunction with nitrogen and oxygen plasmas is utilized to deposit the AlN and Al_2O_3 layers at growth rates of 0.61 and 1.05 Å/cycle, respectively. A deposition temperature of 350 °C is used during the growth of all samples.

III. CHARACTERIZATION

We characterize the structural and chemical compositions of the AMLs and control films by the following techniques: transmission electron microscopy (TEM) [23], scanning transmission electron microscopy coupled with electron energy loss spectroscopy (STEM-EELS) [24–26], and x-ray reflectivity (XRR) [27]. The findings of these characterization techniques along with the measured sound speed and thermal conductivity of the samples are provided in Table I. Details of the characterization techniques can be found in the Supplemental Material [28].

TEM is used to characterize the period and film thickness of the AlN/Al_2O_3 multilayers and control samples. TEM images exhibiting the periodicity of the 22- and 2.4-nm AMLs are presented in Figs. 1(a) and 1(b), respectively. The final thicknesses of the four multilayer samples are within 15% of each other (95–109 nm). The top period of the multilayers is asymmetrically deposited, while the rest of the periods are symmetric. The AlN layers of the 22- and 10-nm-period multilayers contain nanometer-sized crystalline grains. Grains of similar sizes have also been detected in the a-AlN control samples. However, no such nanocrystals are observed in the 5- and 2.4-nm-period multilayers or the a-Al_2O_3 control samples.

To determine the relative chemical composition of the AlN and Al_2O_3 layers, we perform STEM-EELS characterization on the 22-, 5-, and 2.4-nm-period multilayers. The periodic variations of the nitrogen and oxygen content in these three multilayers are shown in Figs. 1(c), 1(d), and 1(e), respectively. In the 22-nm-period multilayer, the Al_2O_3 layers do not contain any nitrogen. The AlN layers, on the other hand, contain ∼15 at. % oxygen relative to nitrogen. In crystalline AlN, incorporated oxygen impurities have been shown to readily react and substitute the nitrogen [29–31]. The same mechanism of oxidation allows us to grow amorphous AlN/Al_2O_3 multilayers with varying oxygen stoichiometry

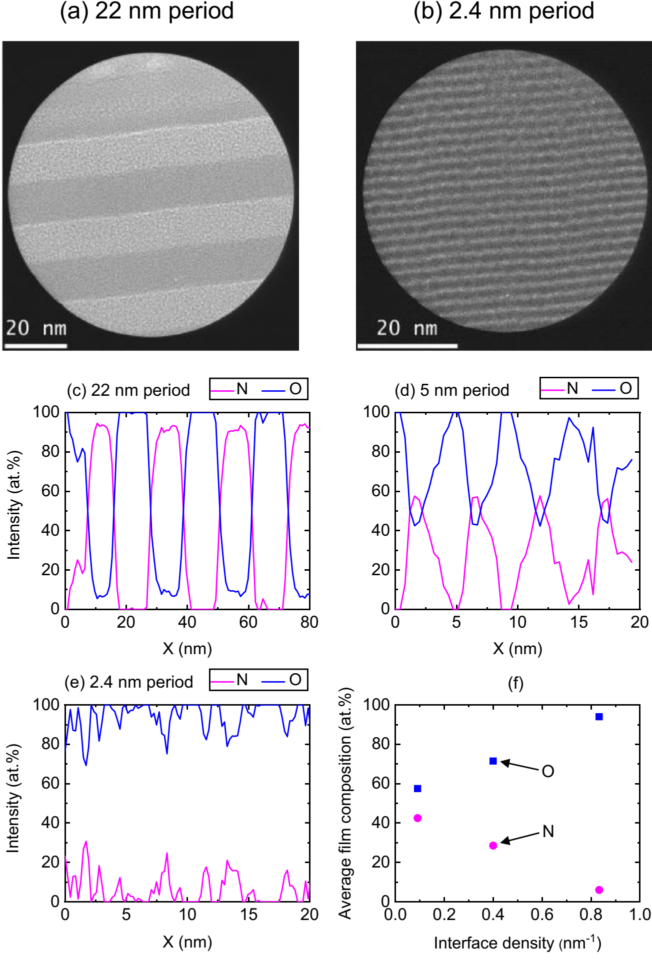

FIG. 1. TEM images of the (a) 22- and (b) 2.4-nm-period AMLs. Relative at. % of oxygen (O) and nitrogen (N) in the (c) 22-, (d) 5-, and (e) 2.4-nm-period multilayers quantified from STEM-EELS line scans. (f) Average film composition as a function of interface density of the AMLs.

in the AlN layers. Due to this tendency of AlN to oxidize during growth, the AlN/Al_2O_3 interface is chemically diffuse in the 22-nm-period sample. The extent of oxidation is more severe in the 5-nm-period multilayer. In this specimen, the oxygen composition continuously varies in a sinusoidal-like behavior with a maximum of 100 at. % in the Al_2O_3 layer and a minimum of ∼43 at. % in the AlN layer. In the 2.4-nm-period multilayer, the nitrogen content in the AlN layer is very low, and the average film composition is ∼94 at. % oxygen relative to nitrogen. This gradual reduction in the nitrogen content of the AlN layer as a function of interface density (i.e., 2/period thickness) is more clearly exhibited in Fig. 1(f). From this figure, we can also reasonably estimate that the average film composition of the 10-nm-period multilayer is ∼62.4 at. % oxygen relative to nitrogen. We further note that the presence of some nonstoichiometric Al_2O_3 can be expected in the AlN layers of our multilayers [29–31]. However, within the experimental resolution of our technique, we are unable to determine the relative percentage of any nonstoichiometry in the studied samples.

As the thermal conductivity of amorphous materials highly depends on density [32,33], we use XRR to measure the density of the specimens. The XRR-measured densities of the a-AlN and a-Al_2O_3 control samples are approximately 2.6 and 3.08 g/cm^3, respectively. Similar values have been reported in the literature for a-AlN and a-Al_2O_3 [19]. Extracting the density of the AlN/Al_2O_3 multilayers from XRR is challenging due to the compositional change with interface density. Therefore, based on the density of the control films, we assume that the AMLs have an average density of $\sim 2.84 \pm 0.24$ g/cm^3. This assumption is verified in Sec. IV.

IV. RESULTS AND DISCUSSION

To investigate the effects of structural and chemical disorder on the sound speed of the AMLs, we employ the picosecond acoustics technique [14,22,32,34–37]. For this purpose, we use a two-tint time-domain thermoreflectance (TDTR) setup, details of which are provided in the Supplemental Material [28,38–42]. Prior to the measurements, an ∼80-nm aluminum (Al) film is deposited atop the samples via electron beam evaporation for optothermal transduction [43–47]. During picosecond acoustics, the heating event from the pump laser launches a strain wave that propagates through the Al and underlying amorphous films at the corresponding longitudinal sound speed of each film. The interfaces partially reflect this strain wave, which is captured by the probe beam at earlier pump-probe delay times. A “hump” or “trough” is generated in the TDTR thermal decay curves based on whether the reflecting material possesses a higher or lower acoustic impedance, respectively. With the knowledge of the propagation time period and film thickness, the longitudinal sound speed of the amorphous films can be calculated. Additional details regarding the picosecond acoustics technique and analyses can be found in the Supplemental Material [28].

Figure 2(a) shows the ratios of in-phase to out-of-phase signal ($-V_{in}/V_{out}$) in the picosecond regime for the 81-nm-period a-AlN, 86-nm-period a-Al_2O_3, and 22-nm-period AlN/Al_2O_3 multilayer films. The differences in acoustic impedance among the Al transducer, amorphous films, and Si substrate are clearly discernible here through the humps and troughs. The measured longitudinal sound speed of the amorphous films as a function of interface density is exhibited in Fig. 2(b). As shown here, the a-AlN and a-Al_2O_3 control films possess a longitudinal sound speed of 6370 ± 547 and 8750 ± 328 m/s, respectively. While the longitudinal sound speed of a-AlN has not been reported in the literature, our measured value of a-Al_2O_3 is in excellent agreement with the findings of Gorham *et al.* [32]. For the AlN/Al_2O_3 multilayers, the longitudinal sound speed increases with interface density. To understand the origin of this behavior, we review the relationship between the longitudinal sound speed and chemical composition of the multilayer films in Fig. 2(c). The longitudinal sound speed of the AMLs scales linearly with the oxygen content and agrees with the predictions of rule of mixtures. As the Al-O bond is significantly stronger than the Al-N bond [48–51], with increasing oxygen content, the number of Al-O bonds increases, leading to elastic stiffening [22] and the observed trend in longitudinal sound speed. Figures 2(b) and

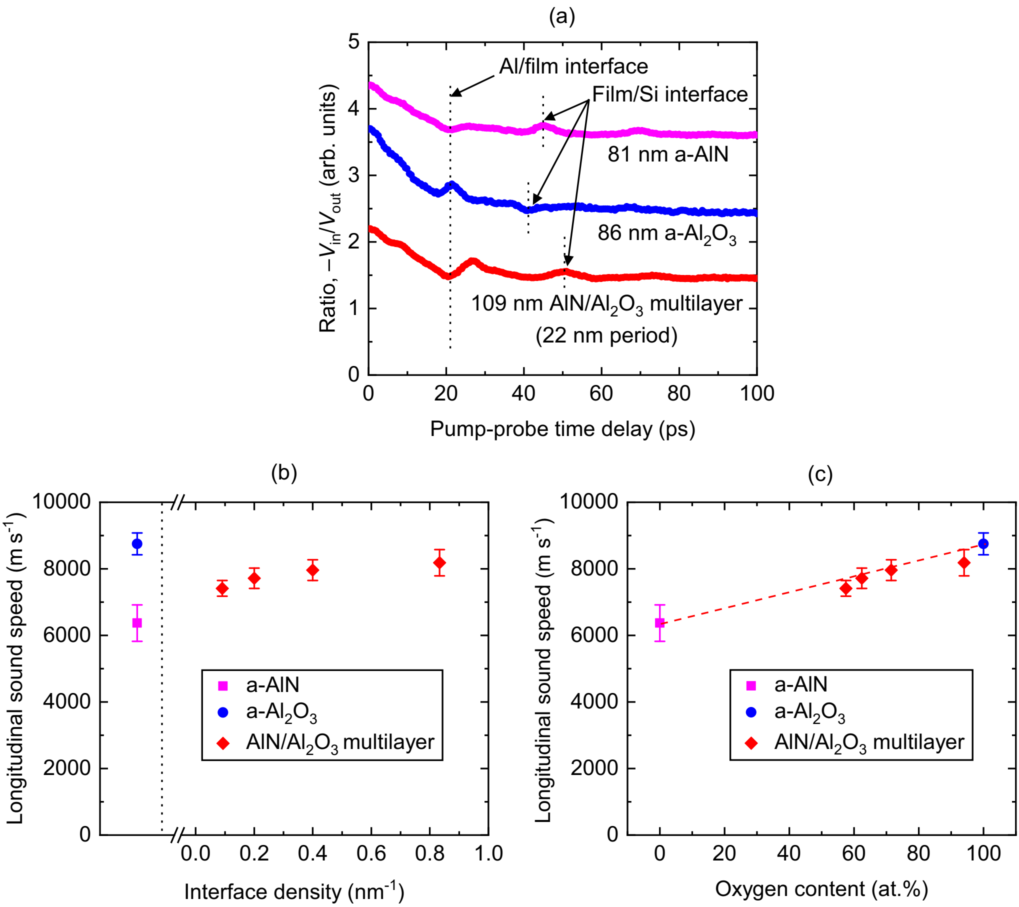

FIG. 2. (a) Picosecond acoustic response of TDTR measurements for a-AlN, a-Al_2O_3, and AlN/Al_2O_3 multilayer films. (b) and (c) represent longitudinal sound speed of the amorphous films as a function of interface density and oxygen content, respectively. The dashed line in (c) represents the longitudinal sound speed predicted via the rule of mixtures based on the composition of the AMLs.

2(c) provide evidence that instead of the number of interfaces, the chemical composition is dictating the longitudinal sound speed of the AMLs used in this study.

In Figs. 3(a) and 3(b), we present the TDTR-measured cross-plane thermal conductivity of the amorphous films as a function of interface density and oxygen content, respectively. For analyzing the multilayer TDTR data, we assume a volumetric heat capacity of $\sim 2.17 \pm 0.19$ MJ m^{-3} K^{-1} based on the literature-reported [52] specific heat capacity and estimated density of the AMLs. To evaluate the validity of

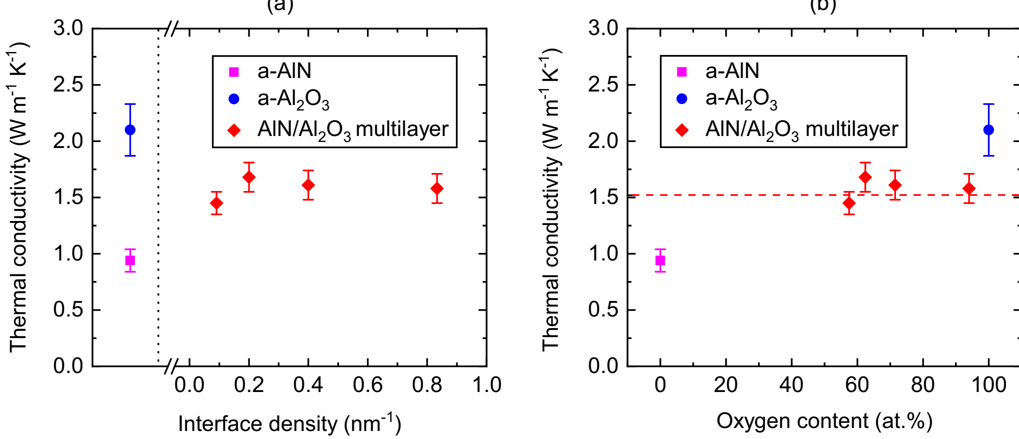

FIG. 3. TDTR-measured cross-plane thermal conductivity of a-AlN, a-Al_2O_3, and AlN/Al_2O_3 multilayer films as a function of (a) interface density and (b) oxygen content. The dashed line in (b) represents the average thermal conductivity of a-AlN and a-Al_2O_3 control films.

this assumption, we measure the thermal conductivity of the AMLs with steady-state thermoreflectance (SSTR), a thermometry technique insensitive to heat capacity [53–56]. As shown in Fig. S2 of the Supplemental Material, the TDTR- and SSTR-measured values are in excellent agreement, thus proving the accuracy of our assumed volumetric heat capacity and density. Details of our TDTR and SSTR measurement procedures and analyses are provided in the Supplemental Material [28,57–63].

As shown in Fig. 3, the thermal conductivity of the AMLs is nearly the average of that of a-AlN and a-Al_2O_3 and remains constant as a function of both interface density and oxygen content. As the composition of the AMLs is changing, a simple average between the two constituents cannot explain the thermal conductivity data. We hypothesize that two opposing thermal transport mechanisms are taking place simultaneously in the AlN/Al_2O_3 multilayers, leading to the observed trend. First, the thermal conductivity of the AMLs is expected to decrease with interface density as the thermal resistance due to the interfaces becomes greater. Similar behavior has been observed in amorphous Si/Ge [18] and Al_2O_3/TiO_2 [17] multilayers. Second, the thermal conductivity of the AMLs is expected to increase with the oxygen content of the film. As the thermal conductivity of a-Al_2O_3 is higher compared with a-AlN, the higher oxygen content would reduce the net resistance provided by a period [14,64]. We posit that due to such opposing influence of interface density and oxygen content, the thermal conductivity of the AMLs remains nearly constant.

To study our hypothesis, we use molecular dynamics to investigate the influence of interface density and composition on the thermal conductivity of an AML. Since an empirical potential of a-AlN or a-Al_2O_3 is not available in the literature, we use amorphous Si/Ge multilayers as a representative system. The MD predicted thermal conductivity of a-Si and a-Ge is 1.33 ± 0.13 and 0.72 ± 0.07 W m^{-1} K^{-1}, respectively. These thermal conductivity values are in agreement with the literature [18,65,66]. To mimic the compositionally variant AMLs studied in this paper, we simulate the Si/Ge multilayers for three distinct cases. In the first case, the amorphous Si/Ge multilayers possess sharp interfaces with equal Si and Ge contents. In the second case, the interfaces between the a-Si and a-Ge layers possess significant intermixing. In the third case, the a-Si layer is much thicker compared with the a-Ge layer representing a higher Si content in the system. Details of our MD simulations are provided in the Supplemental Material [28,67–74].

Figures 4(a)–4(c) show the schematics of the computational domains for the three cases. The thermal conductivity as a function of interface density for these cases is presented in Fig. 4(d). As exhibited here, when the Si/Ge multilayer has sharp interfaces with equal Si and Ge contents, the thermal conductivity decreases with interface density due to the non-negligible role of the interface. This supports our hypothesis regarding the role of interfacial resistance in the thermal conductivity of AMLs. The influence of the interfaces remains nearly the same regardless of significant intermixing at the interfaces. This indicates that the chemically diffuse interfaces observed in this paper cannot alone account for the near-constant thermal conductivity. However, for the same

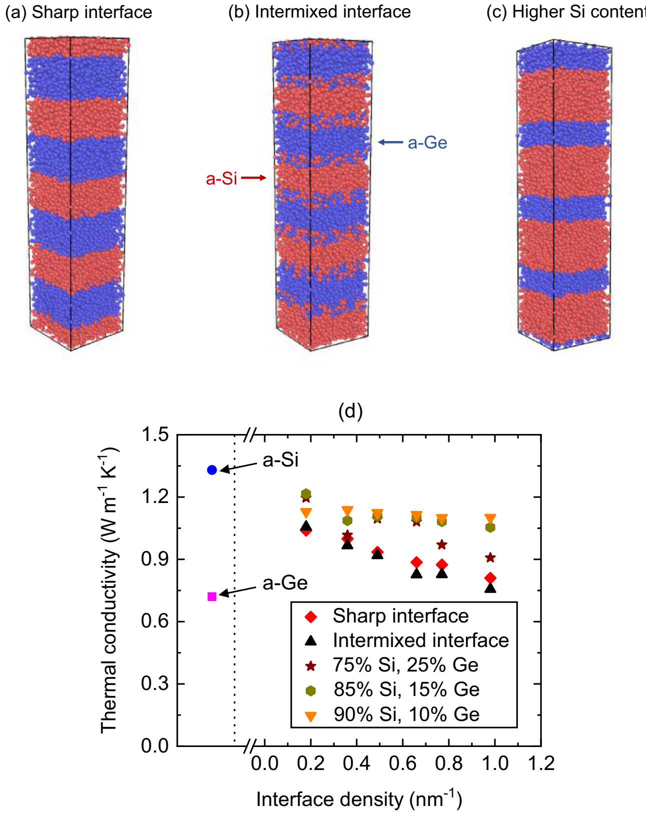

FIG. 4. Schematics of the computational domains for an amorphous Si/Ge multilayer corresponding to three cases: (a) sharp interface, (b) intermixed interface, and (c) higher Si content. (d) Thermal conductivity as a function of interface density for the domains presented in (a)–(c). The error bars associated with these thermal conductivity values are ∼10%.

interface density, when the Si layer is thicker, the thermal conductivity is usually higher. Increasing the Si content from 75 to 90% leads to an increase in thermal conductivity, particularly for higher interface densities. This happens as the thicker Si layer reduces the net resistance provided by the multilayer period. Thus these simulations at least qualitatively suggest that the thermal conductivity of AMLs can be highly affected by composition along with interface density. The opposing influence of the composition and interface density in amorphous Si/Ge multilayers can also be explained by diffusive thermal transport as shown in Sec. S7 of the Supplemental Material [28,65,75–78].

V. CONCLUSION

In summary, we investigate the impact of structural and chemical disorder on the sound speed and thermal conductivity of a series of amorphous AlN/Al_2O_3 multilayers. The oxygen content of these AMLs linearly increases with interface density due to oxidation of the AlN layers during growth. As the Al-O bond is stronger than the Al-N bond, the longitudinal sound speed of the multilayers linearly increases with oxygen content and is independent of interface density. However, the thermal conductivity of multilayers is impacted by both interface density and oxygen content. These two

parameters act to decrease and increase the thermal conductivity, respectively. Due to such opposing influences, the thermal conductivity of the AlN/Al_2O_3 multilayers is the average of that of a-AlN and a-Al_2O_3 and remains nearly constant. We further verify this by performing molecular dynamics simulations on a representative Si/Ge system. Our study shows that structural and chemical disorder can have vastly different effects on the sound speed and thermal conductivity of an AML.

ACKNOWLEDGMENTS

The authors acknowledge financial support from the Semiconductor Research Corporation, Grant No. 2021-NM-3047, and ONR MURI Program, Grant No. N00014-18-1-2429. C.J.D. and A.G. thank the ONR, Grant No. N00014-21-1-2622, for support. This work is supported, in part, by the Laboratory Directed Research and Development Program at Sandia National Laboratories, a multimission laboratory managed and operated by National Technology and Engineering Solutions of Sandia, LLC, a wholly owned subsidiary of Honeywell International, Inc., for the U.S. Department of Energy's National Nuclear Security Administration under Contract No. DE-NA0003525. Any subjective views or opinions that might be expressed in the paper do not necessarily represent the views of the U.S. Department of Energy or the United States Government.

[1] N. P. Padture, M. Gell, and E. H. Jordan, Science **296**, 280 (2002).

[2] E. Bertran, G. Viera, E. Martinez, J. Esteve, Y. Maniette, J. Farjas, and P. Roura, Thin Solid Films **377-378**, 495 (2000).

[3] H. Steibig, R. Street, D. Knipp, M. Krause, and J. Ho, Appl. Phys. Lett. **88**, 013509 (2006).

[4] D. Caputo, G. de Cesare, A. Nascetti, and M. Tucci, IEEE Trans. Electron Devices **55**, 452 (2007).

[5] H. Ohta, R. Huang, and Y. Ikuhara, Phys. Status Solidi RRL **2**, 105 (2008).

[6] M. Mazumder, T. Borca-Tasciuc, S. C. Teehan, E. Stinzianni, H. Efstathiadis, and S. Solovyov, Appl. Phys. Lett. **96**, 093103 (2010).

[7] M. S. Akhanda, S. E. Rezaei, K. Esfarjani, S. Krylyuk, A. V. Davydov, and M. Zebarjadi, Phys. Rev. Mater. **5**, 015403 (2021).

[8] M. A. Maruf, S. M. M. Rizvi, M. Noor-A-Alam, D. Shin, W. Haider, and I. Shabib, Prog. Nat. Sci.: Mater. Int. **31**, 688 (2021).

[9] M. A. Maruf, M. Noor-A-Alam, W. Haider, and I. Shabib, Mater. Chem. Phys. **285**, 126171 (2022).

[10] Y. Liao, S. Iwamoto, M. Sasaki, M. Goto, and J. Shiomi, Nano Energy **84**, 105903 (2021).

[11] A. Giri, J. L. Braun, and P. E. Hopkins, J. Appl. Phys. **119**, 235305 (2016).

[12] A. Giri, B. F. Donovan, and P. E. Hopkins, Phys. Rev. Mater. **2**, 056002 (2018).

[13] R. Anufriev, S. Tachikawa, S. Gluchko, Y. Nakayama, T. Kawamura, L. Jalabert, and M. Nomura, Appl. Phys. Lett. **117**, 093103 (2020).

[14] J. L. Braun, S. W. King, A. Giri, J. T. Gaskins, M. Sato, T. Fujiseki, H. Fujiwara, and P. E. Hopkins, Appl. Phys. Lett. **109**, 191905 (2016).

[15] A. Giri, S. W. King, W. A. Lanford, A. B. Mei, D. Merrill, L. Li, R. Oviedo, J. Richards, D. H. Olson, J. L. Braun, J. T. Gaskins, F. Deangelis, A. Henry, and P. E. Hopkins, Adv. Mater. **30**, 1804097 (2018).

[16] M. E. DeCoster, X. Chen, K. Zhang, C. M. Rost, E. R. Hoglund, J. M. Howe, T. E. Beechem, H. Baumgart, and P. E. Hopkins, Adv. Funct. Mater. **29**, 1904073 (2019).

[17] S. Ali, T. Juntunen, S. Sintonen, O. M. Ylivaara, R. L. Puurunen, H. Lipsanen, I. Tittonen, and S.-P. Hannula, Nanotechnology **27**, 445704 (2016).

[18] A. Giri, P. E. Hopkins, J. G. Wessel, and J. C. Duda, J. Appl. Phys. **118**, 165303 (2015).

[19] J. T. Gaskins, P. E. Hopkins, D. R. Merrill, S. R. Bauers, E. Hadland, D. C. Johnson, D. Koh, J. H. Yum, S. Banerjee, B. J. Nordell, M. M. Paquette, A. N. Caruso, W. A. Lanford, P. Henry, L. Ross, H. Li, L. Li, M. French, A. M. Rudolph, and S. W. King, ECS J. Solid State Sci. Technol. **6**, N189 (2017).

[20] J. L. Braun, S. W. King, E. R. Hoglund, M. A. Gharacheh, E. A. Scott, A. Giri, J. A. Tomko, J. T. Gaskins, A. Al-Kukhun, G. Bhattarai, M. M. Paquette, G. Chollon, B. Willey, G. A. Antonelli, D. W. Gidley, J. Hwang, J. M. Howe, and P. E. Hopkins, Phys. Rev. Mater. **5**, 035604 (2021).

[21] X. Wang, V. Ho, R. A. Segalman, and D. G. Cahill, Macromolecules **46**, 4937 (2013).

[22] J. L. Braun, C. M. Rost, M. Lim, A. Giri, D. H. Olson, G. N. Kotsonis, G. Stan, D. W. Brenner, J.-P. Maria, and P. E. Hopkins, Adv. Mater. **30**, 1805004 (2018).

[23] R. Gauvin, in *Materials Characterization and Optical Probe Techniques: A Critical Review*, Proceedings of SPIE Vol. 10291 (International Society for Optics and Photonics, Bellingham, WA, 1997), p. 102910C.

[24] W. Grogger, F. Hofer, G. Kothleitner, and B. Schaffer, Top. Catal. **50**, 200 (2008).

[25] M. Varela, J. Gazquez, and S. J. Pennycook, MRS Bull. **37**, 29 (2012).

[26] F. De la Peña, V. Fauske, P. Burdet, E. Prestat, P. Jokubauskas, M. Nord, T. Ostasevicius, K. MacArthur, M. Sarahan, D. Johnstone, J. Taillon, A. Eljarrat, V. Migunov, J. Caron, T. Furnival, S. Mazzucco, T. Aarholt, M. Walls, T. Slater, F. Winkler *et al.*, 2018, https://doi.org/10.5281/zenodo.1469364.

[27] M. Yasaka, X-ray thin-film measurement techniques, The Rigaku Journal, **26**, 1 (2010).

[28] See Supplemental Material at http://link.aps.org/supplemental/10.1103/PhysRevMaterials.7.025401 for detailed descriptions of STEM-EELS, XRR, TDTR, SSTR, picosecond acoustics, uncertainty analysis, MD simulations, and diffusive thermal transport.

[29] G. A. Slack, J. Phys. Chem. Solids **34**, 321 (1973).

[30] G. A. Slack, R. A. Tanzilli, R. Pohl, and J. Vandersande, J. Phys. Chem. Solids **48**, 641 (1987).

[31] G. A. Slack, L. J. Schowalter, D. Morelli, and J. A. Freitas Jr, J. Cryst. Growth **246**, 287 (2002).

[32] C. S. Gorham, J. T. Gaskins, G. N. Parsons, M. D. Losego, and P. E. Hopkins, Appl. Phys. Lett. **104**, 253107 (2014).

[33] E. A. Scott, J. T. Gaskins, S. W. King, and P. E. Hopkins, APL Mater. **6**, 058302 (2018).

[34] H. McSkimin, J. Appl. Phys. **24**, 988 (1953).

[35] Electrochemical series *in CRC Handbook of Chemistry and Physics*, 85th ed., edited by D. R. Lide (CRC, Boca Raton, FL, 2004).

[36] G. T. Hohensee, W.-P. Hsieh, M. D. Losego, and D. G. Cahill, Rev. Sci. Instrum. **83**, 114902 (2012).

[37] K. Aryana, J. T. Gaskins, J. Nag, D. A. Stewart, Z. Bai, S. Mukhopadhyay, J. C. Read, D. H. Olson, E. R. Hoglund, J. M. Howe, A. Giri, M. K. Grobis, and P. E. Hopkins, Nat. Commun. **12**, 774 (2021).

[38] D. H. Olson, J. T. Gaskins, J. A. Tomko, E. J. Opila, R. A. Golden, G. J. Harrington, A. L. Chamberlain, and P. E. Hopkins, Scr. Mater. **177**, 214 (2020).

[39] A. Giri, A. Z. Chen, A. Mattoni, K. Aryana, D. Zhang, X. Hu, S.-H. Lee, J. J. Choi, and P. E. Hopkins, Nano Lett. **20**, 3331 (2020).

[40] Y. R. Koh, M. S. B. Hoque, H. Ahmad, D. H. Olson, Z. Liu, J. Shi, Y. Wang, K. Huynh, E. R. Hoglund, K. Aryana, J. M. Howe, M. S. Goorsky, S. Graham, T. Luo, J. K. Hite, W. A. Doolittle, and P. E. Hopkins, Phys. Rev. Mater. **5**, 104604 (2021).

[41] K. Aryana, Y. Zhang, J. A. Tomko, M. S. B. Hoque, E. R. Hoglund, D. H. Olson, J. Nag, J. C. Read, C. Ríos, J. Hu, and P. E. Hopkins, Nat. Commun. **12**, 7187 (2021).

[42] K. Aryana, D. A. Stewart, J. T. Gaskins, J. Nag, J. C. Read, D. H. Olson, M. K. Grobis, and P. E. Hopkins, Nat. Commun. **12**, 2817 (2021).

[43] Y. Wang, J. Y. Park, Y. K. Koh, and D. G. Cahill, J. Appl. Phys. **108**, 043507 (2010).

[44] R. Wilson, B. A. Apgar, L. W. Martin, and D. G. Cahill, Opt. Express **20**, 28829 (2012).

[45] C. M. Rost, J. Braun, K. Ferri, L. Backman, A. Giri, E. J. Opila, J.-P. Maria, and P. E. Hopkins, Appl. Phys. Lett. **111**, 151902 (2017).

[46] L. Wang, R. Cheaito, J. Braun, A. Giri, and P. Hopkins, Rev. Sci. Instrum. **87**, 094902 (2016).

[47] E. L. Radue, J. A. Tomko, A. Giri, J. L. Braun, X. Zhou, O. V. Prezhdo, E. L. Runnerstrom, J.-P. Maria, and P. E. Hopkins, ACS Photonics **5**, 4880 (2018).

[48] T. Cottrell, *The Strengths of Chemical Bonds*, 2nd ed. (Butterworths, London, 1958).

[49] S. W. Benson, J. Chem. Educ. **42**, 502 (1965).

[50] J. Kerr, Chem. Rev. **66**, 465 (1966).

[51] B. deB. Darwent, National Standard Reference Data Series No. 31 (1970).

[52] Y. Touloukian and E. Buyco, *Specific Heat-Nonmetallic Solids*, Thermophysical Properties of Matter–The TPRC Data Series Vol. 5 (Thermophysical and Electronic Properties Information Analysis Center, Lafayette, IN, 1970).

[53] M. Qin, J. Gild, C. Hu, H. Wang, M. S. B. Hoque, J. L. Braun, T. J. Harrington, P. E. Hopkins, K. S. Vecchio, and J. Luo, J. Eur. Ceram. Soc. **40**, 5037 (2020).

[54] M. S. B. Hoque, Y. R. Koh, K. Aryana, E. R. Hoglund, J. L. Braun, D. H. Olson, J. T. Gaskins, H. Ahmad, M. M. M. Elahi, J. K. Hite, Z. C. Leseman, W. A. Doolittle, and P. E. Hopkins, Rev. Sci. Instrum. **92**, 064906 (2021).

[55] M. S. B. Hoque, Y. R. Koh, J. L. Braun, A. Mamun, Z. Liu, K. Huynh, M. E. Liao, K. Hussain, Z. Cheng, E. R. Hoglund, D. H. Olson, J. A. Tomko, K. Aryana, R. Galib, J. T. Gaskins, M. M. M. Elahi, Z. C. Leseman, J. M. Howe, T. Luo, S. Graham *et al.*, ACS Nano **15**, 9588 (2021).

[56] J. L. Braun, D. H. Olson, J. T. Gaskins, and P. E. Hopkins, Rev. Sci. Instrum. **90**, 024905 (2019).

[57] P. E. Hopkins, Int. Scholarly Res. Not. **2013**, 682586 (2013).

[58] C. S. Gorham, K. Hattar, R. Cheaito, J. C. Duda, J. T. Gaskins, T. E. Beechem, J. F. Ihlefeld, L. B. Biedermann, E. S. Piekos, D. L. Medlin, and P. E. Hopkins, Phys. Rev. B **90**, 024301 (2014).

[59] C. Monachon, L. Weber, and C. Dames, Annu. Rev. Mater. Res. **46**, 433 (2016).

[60] C. Cancellieri, E. A. Scott, J. Braun, S. W. King, R. Oviedo, C. Jezewski, J. Richards, F. La Mattina, L. P. Jeurgens, and P. E. Hopkins, J. Appl. Phys. **128**, 195302 (2020).

[61] J. T. Gaskins, G. Kotsonis, A. Giri, S. Ju, A. Rohskopf, Y. Wang, T. Bai, E. Sachet, C. T. Shelton, Z. Liu, Z. Cheng, B. M. Foley, S. Graham, T. Luo, A. Henry, M. S. Goorsky, J. Shiomi, J.-P. Maria, and P. E. Hopkins, Nano Lett. **18**, 7469 (2018).

[62] A. Giri and P. E. Hopkins, Adv. Funct. Mater. **30**, 1903857 (2020).

[63] Y. R. Koh, J. Shi, B. Wang, R. Hu, H. Ahmad, S. Kerdsongpanya, E. Milosevic, W. A. Doolittle, D. Gall, Z. Tian, S. Graham, and P. E. Hopkins, Phys. Rev. B **102**, 205304 (2020).

[64] M. G. Ghossoub, J.-H. Lee, O. T. Baris, D. G. Cahill, and S. Sinha, Phys. Rev. B **82**, 195441 (2010).

[65] J. L. Braun, C. H. Baker, A. Giri, M. Elahi, K. Artyushkova, T. E. Beechem, P. M. Norris, Z. C. Leseman, J. T. Gaskins, and P. E. Hopkins, Phys. Rev. B **93**, 140201(R) (2016).

[66] S. Kwon, J. Zheng, M. C. Wingert, S. Cui, and R. Chen, ACS Nano **11**, 2470 (2017).

[67] S. Plimpton, J. Comput. Phys. **117**, 1 (1995).

[68] M. Ishimaru, S. Munetoh, and T. Motooka, Phys. Rev. B **56**, 15133 (1997).

[69] J. M. Larkin and A. J. H. McGaughey, Phys. Rev. B **89**, 144303 (2014).

[70] J. L. Feldman, P. B. Allen, and S. R. Bickham, Phys. Rev. B **59**, 3551 (1999).

[71] A. J. McGaughey and M. Kaviany, Adv. Heat Transfer **39**, 169 (2006).

[72] A. McGaughey and M. Kaviany, Int. J. Heat Mass Transfer **47**, 1783 (2004).

[73] M. P. Allen and D. J. Tildesley, *Computer Simulation of Liquids* (Oxford University Press, Oxford, 2017).

[74] P. K. Schelling, S. R. Phillpot, and P. Keblinski, Phys. Rev. B **65**, 144306 (2002).

[75] T. Borca-Tasciuc, W. Liu, J. Liu, T. Zeng, D. W. Song, C. D. Moore, G. Chen, K. L. Wang, M. S. Goorsky, T. Radetic, R. Gronsky, T. Koga, and M. S. Dresselhaus, Superlattices Microstruct. **28**, 199 (2000).

[76] S. Shenogin, A. Bodapati, P. Keblinski, and A. J. McGaughey, J. Appl. Phys. **105**, 034906 (2009).

[77] K. T. Regner, D. P. Sellan, Z. Su, C. H. Amon, A. J. McGaughey, and J. A. Malen, Nat. Commun. **4**, 1640 (2013).

[78] A. Giri, J. L. Braun, D. M. Shima, S. Addamane, G. Balakrishnan, and P. E. Hopkins, J. Phys. Chem. C **122**, 29577 (2018).